Article

Oxygen Vacancy Density Dependence with a Hopping Conduction Mechanism in Multilevel Switching Behavior of HfO$_2$-Based Resistive Random Access Memory Devices

Desmond J. J. Loy, Putu A. Dananjaya, Somsubhra Chakrabarti, Kuan Hong Tan, Samuel C. W. Chow, Eng Huat Toh, and Wen Siang Lew*

Read Online

ACCESS | Metrics & More | Article Recommendations

ABSTRACT: We report a switching model that directly explains the change in activation energy (E_{AC}) at different RESET stop voltages (V_{stop}) in HfO$_2$-based resistive random access memory devices. The dependence of oxygen vacancy-driven conductive filaments (V_o^{2+}) density (n_D) on V_{stop} was validated by a kinetic Monte Carlo (kMC) simulation and hopping conduction mechanism. A wide operating range of temperatures from −40 to 175 °C is achieved with stable endurance of 100 ns short pulses and high retention of more than 10 years at 125 °C. Distinct exponentially increased multilevel high-resistance states are observed at increasing V_{stop} and is attributed to the increase in E_{AC} with V_{stop}. The increase in E_{AC} due to the increase in V_{stop} and depletion of n_D during RESET was explained using our proposed switching model. A kMC simulation further emphasizes this relation due to the depletion of V_o^{2+} during RESET, which was supported by the increase in trap-to-trap distance in the hopping conduction analysis.

KEYWORDS: RRAM, oxygen vacancy density, kinetic Monte Carlo, hopping conduction, high retention, multilevel switching, activation energy, wide operating temperature range
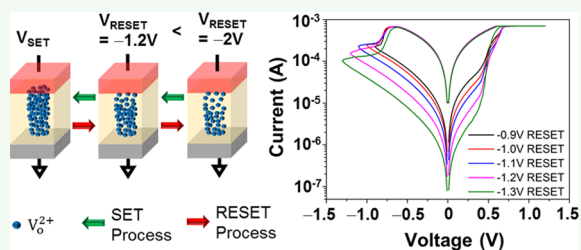
■ INTRODUCTION

Resistive random access memory (RRAM) has been one of the most optimistic non-volatile memories,[1−3] largely attributed to its simple metal−insulator−metal (MIM) structure, high speed and low power, high scalability, high density, and high endurance and retention capabilities, along with its high complementary metal oxide semiconductor (CMOS) compatibility.[4−6] Oxide-based RRAM devices are the most widely studied due to their dielectric properties in MIM structures in creating memory states from the commonly investigated metallic or oxygen vacancy-driven conductive filaments (V_o^{2+}).[7−9] The details of these switching mechanisms are being debated, but there is strong evidence where device, stack, and/or thickness engineering could alter the switching mechanism of the RRAM.[10−12] Among all the oxides, high-k HfO$_x$ is widely studied as it is CMOS friendly and has been established as gate dielectrics in state-of-the-art logic and memory devices. HfO$_x$ is also a great candidate due its good thermal stability and recently in its multilevel state properties when used as a dielectric of a switching element.[13−17] In traditional memory, there exists two states of "1" and "0", which represents the low resistance state (LRS) and high resistance state (HRS), respectively.[18−20] However, to keep up with the ever-growing digital age where data consumption and generation are growing at an exponential rate, there is an increasingly strong need to advance toward multi-bit to enhance the storage scalability of modern-day memory devices and to delve deeper into neuromorphic applications.[15−17,21−23]

Over the past few decades, there have been numerous works focusing on the modeling studies of multitemperature and multilevel states in resistive switching devices. A physical model and a thermally activated hopping model were proposed by Ielmini for multilevel state filament growth and ion migration.[24] Similarly, a physical model was applied by Bousoulas et al. to highlight the local electric field and temperature profiles of SET/RESET transitions.[25] Numerical models were also proposed by Larentis et al. and Kim et al. to explore temperature and field-accelerated migration of V_o^{2+}.[26,27] Arrhenius equation models were also investigated by Chiu et al. and Khurana et al.[28,29] Furthermore, a negative voltage-modulated multilevel resistive switching during reset was observed and explained using conduction mechanisms by Chakrabarti et al. and Samanta et al.[30,31] On a similar note, temperature-dependent conduction
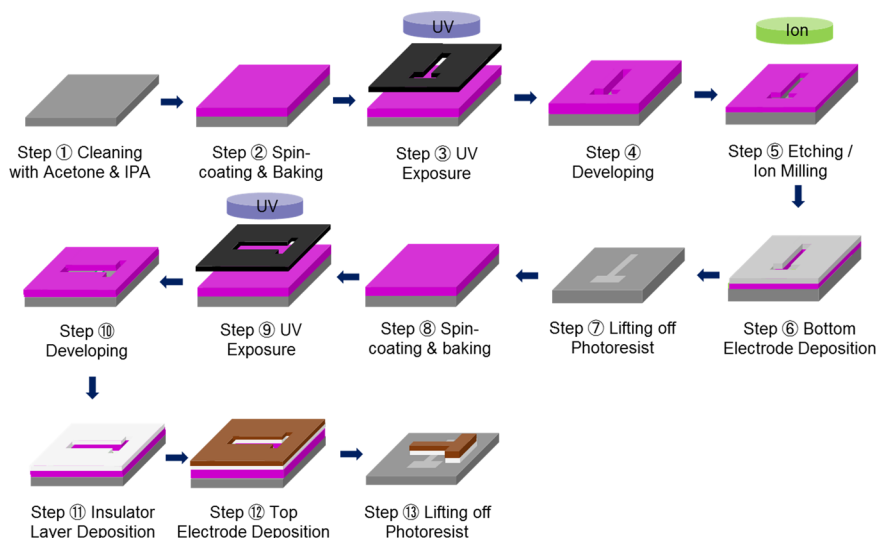
Figure 1. Fabrication process of Pt/HfO$_2$/Ti RRAM devices consisting of a two-step lithography, etching, and deposition processes.
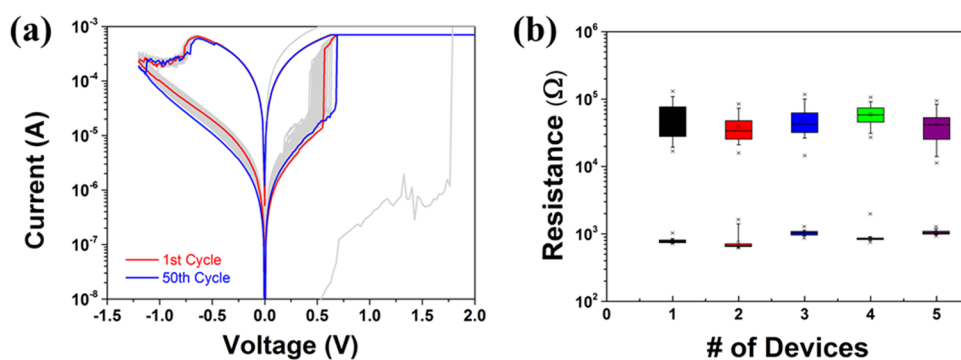
Figure 2. (a) Semi-log $I-V$ plots of Pt/HfO$_2$/Ti resistive switching devices showing the forming process and the first 50 $I-V$ switching cycles at an ON/OFF ratio of ~50×. (b) Resistance box plot of Pt/HfO$_2$/Ti resistive switching devices exhibiting some device-to-device variability.

mechanisms were used by Bai et al. to explain the V_o^{2+} evolution at different multilevel states.[32] A V_o^{2+} evolution model was also proposed by Qi et al. to explain the dendritic filament under different negative electric fields.[33] Although these works of literature exhibit various methods of explaining filament evolution in multilevel states, there have been limited physics understanding on the behavior and density of oxygen vacancies (n_D) at different stopping reset voltages (V_{stop}). Such a study is important because a combination of experimental and theoretical aspects will provide a more comprehensive understanding of filament evolution in multilevel state RRAM.

We validate the multilevel state switching of Pt/HfO$_2$/Ti resistive switching devices with our proposed activation energy (E_{AC}) and V_{stop} switching model in this work. In particular, the E_{AC} of HfO$_2$ can be obtained from an Arrhenius equation fitting and was used to explain the relationship between V_{stop} and n_D. We explored the switching, endurance, and retention characteristics of Pt/HfO$_2$/Ti resistive switching devices to better understand their performance. In addition, TEM and XPS analysis were performed to investigate the uniformity of deposited films and their crystallinity. Temperature studies ranging from −40 to 175 °C were also performed to investigate the $I-V$ characteristics for applications such as automotive and sensors in different weather conditions. Multilevel states were also investigated by varying V_{stop} from −0.9 to −1.3 V at intervals of −0.1 V. A kinetic Monte Carlo (kMC) simulation of Pt/HfO$_2$/Ti RRAMs at various V_{stop} also exhibited an inverse

relation with the number of oxygen vacancies (n_o) at different parts of the filament. This model was further validated by the hopping conduction analysis in the bulk region of the Pt/HfO$_2$/Ti resistive switching devices, where the increments in the trap-to-trap distance (a) were observed with increasing V_{stop}.

EXPERIMENTAL METHODS

Pt(10 nm)/HfO$_2$(10 nm)/Ti(100 nm) resistive switching structures were grown on Si/SiO$_2$ substrates using magnetron sputtering deposition techniques. The chamber base pressure was lower than 2 × 10^{-8} Torr, and the sputter pressure was 2 mTorr with 20 sccm of Ar flow rate. The stacks were patterned into 10 μm × 10 μm devices in a combination of UV lithography and ion-milling processes. A two-step lithography process was used to form a cross pattern of the device junction. These fabrication processes were described in detail from steps 1 to 13 as shown in Figure 1. Current−voltage ($I-V$) measurements were performed using a Keithley 4200 semiconductor parameter analyzer.

CURRENT−VOLTAGE, ENDURANCE, AND RETENTION INVESTIGATIONS OF PT/HFO$_2$/TI RRAM DEVICES

The $I-V$ behavior of Pt/HfO$_2$/Ti resistive switching devices was investigated to better understand the switching characteristics and HRS multilevel switching properties. Consistent switching could be observed in Figure 2a where 50 $I-V$ cycles of one device was plotted. In the 50 $I-V$ cycles, it was found that
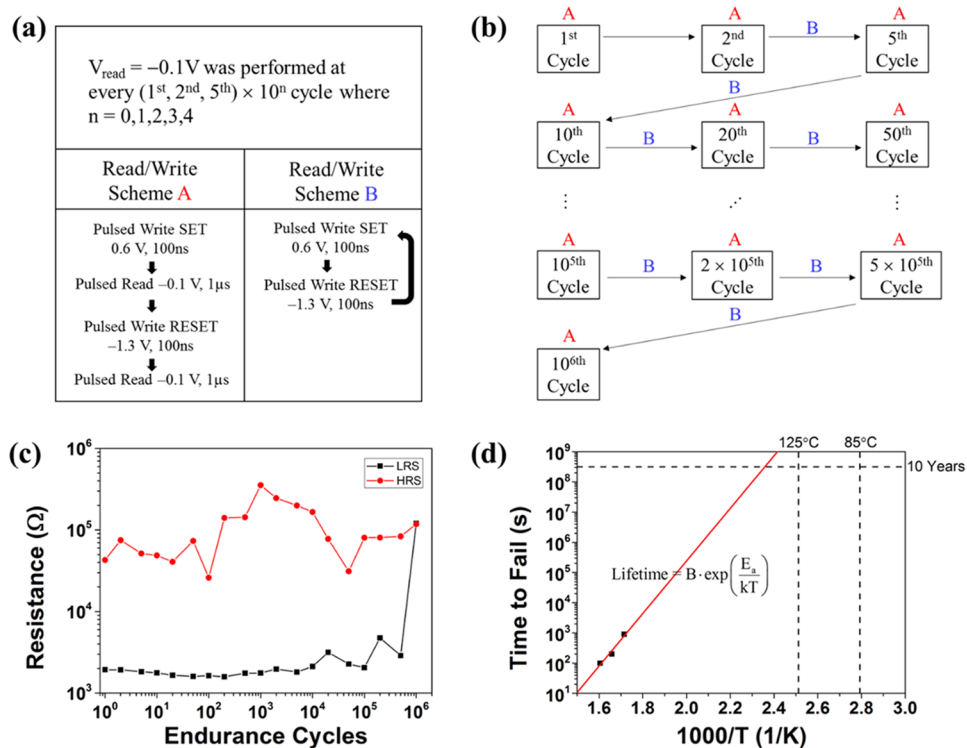
Figure 3. (a) Read/write schemes of endurance performed at SET/RESET pulse heights of 0.6 V/−1.3 V at 100 ns pulse widths. (b) Endurance flow chart where scheme A was implemented to every (1st, 2nd, 5th) × 10^n cycle where $n = 0, 1, 2, 3,$ and 4, while scheme B was implemented to every cycle in between. (c) At least 5×10^5 endurance cycles with an ~50× ON/OFF ratio where LRS converged to the HRS at the 10^6th cycle. (d) Arrhenius plot showing that the retention exceeds 10 years at 125 °C.
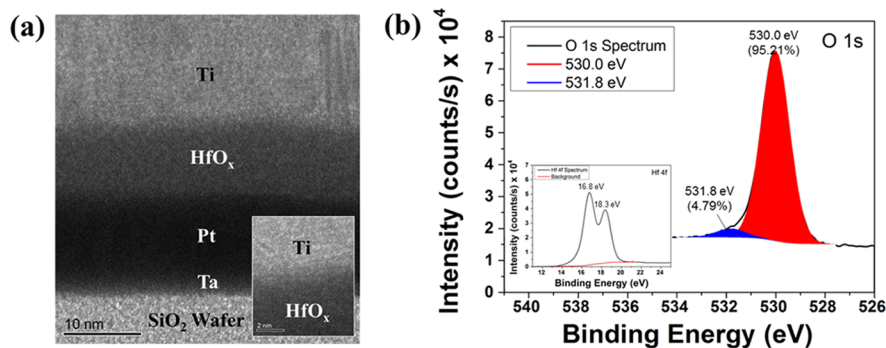
Figure 4. (a) TEM image of Pt/HfO$_2$/Ti resistive switching devices showing uniformly deposited layers. (b) Characteristic XPS profile of O 1s showing two oxygen states indicating 4.79% of oxygen vacancies with the XPS profile of Hf 4f (inset) of HfO$_2$ films.

the average SET voltage is 0.5 V at a compliance current of 700 μA, while the V_{stop} is fixed at −1.2 V, giving an ON/OFF ratio of about 50×. The forming voltage was observed to be at 1.8 V at a compliance current of 1 mA. While there was consistent switching and low cycle-to-cycle variability, it was more important to observe the presence of gradual switching characteristics in the RESET state, thus confirming the existence of multilevel states in the HRS.[34,35] In the investigation of multiple device characteristics, the device-to-device variability of the resistive switching devices with an average SET voltage of 0.5 V and V_{stop} at −1.2 V was also shown in a resistance box plot in Figure 2b, read at −0.1 V. It was found that the median ON/OFF ratio was about 50×, a ratio large enough for multiple level resistance switching states to occur.

Endurance studies were also performed at SET/RESET pulse heights of 0.6 V/−1.3 V at 100 ns pulse widths as shown in the flow chart of Figure 3a. Two read/write schemes A and B were

implemented at different cycles as shown in the flow charts of Figure 3a,b. While scheme A was implemented to every (1st, 2nd, 5th) × 10^n cycle where $n = 0, 1, 2, 3,$ and 4, scheme B was implemented to every cycle in between. Scheme A reads the resistance state after every SET and RESET write, while scheme B adopts a current-blind pulsed voltage stress (PVS) method where there is only SET and RESET writing but no reading.[36] At least 5×10^5 endurance cycles at an average ON/OFF ratio of 50× were observed as the LRS of the 10^6th cycle converged to that of the HRS as shown in Figure 3c, indicating a failure at some point after 5×10^5 endurance cycles. However, these results show that Pt/HfO$_2$/Ti resistive switching devices exhibited a good endurance, an attribute necessary to maintain multilevel HRS switching after multiple endurance cycles.

Retention studies were also performed using an Arrhenius equation where the lifetime of each device is plotted against an inverse of temperature as shown in Figure 3d. The devices were
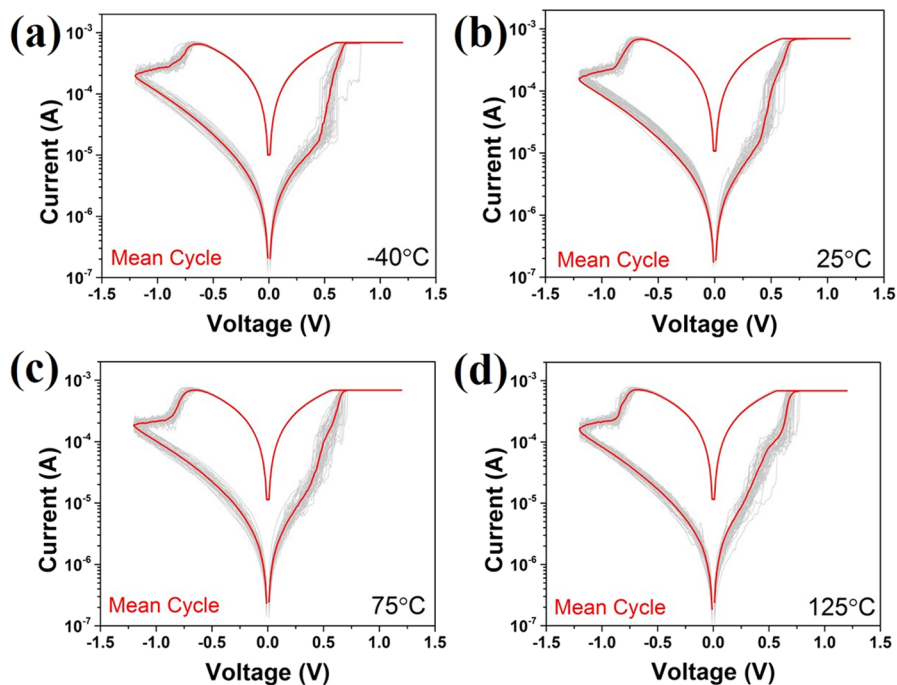
Figure 5. Fifty cycles of semi-log $I-V$ plots of Pt/HfO$_2$/Ti resistive switching devices measured at (a) −40, (b) 25, (c) 75, and (d) 125 °C, with their respective average curves (in red).
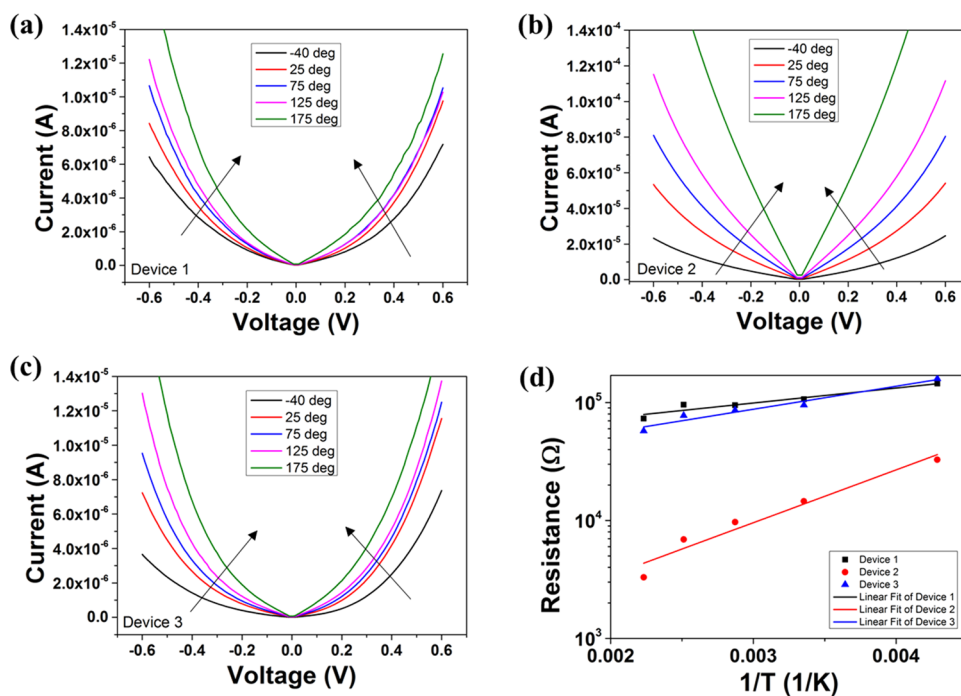
Figure 6. Temperature dependence of $I-V$ curves of (a) device 1, (b) device 2, and (c) device 3. (d) Linearly fitted Arrhenius relationship, R_{HRS} vs. $1/T$ of the devices at different temperatures read at 0.4 V.

first switched to LRS and heated up to 310, 330, and 350 °C while checking their resistance state using a read voltage of −0.1 V. The device is considered failed when the device switched to the HRS unintentionally, and its corresponding time to fail was recorded. These three temperature points were plotted and extrapolated to 10 years (∼3.154 × 10^8 s). From the extrapolation, it was observed that the retention exceeds 10 years at 125 °C, exhibiting strong retention capabilities in Pt/HfO$_2$/Ti RRAM devices. The activation energy ($\underline{E_a}$) was also

extracted to be 1.72 eV, which is higher than 0.6 eV of FLASH.[37] However, the pre-exponential factor B varies with different types of insulators and electrode materials, thus producing different E_a.[6]

■ XPS AND TEM CHARACTERIZATIONS OF PT/HFO$_2$/TI RRAM DEVICES

Material studies such as transmission electron microscopy (TEM) and X-ray photoelectron spectroscopy (XPS) were also
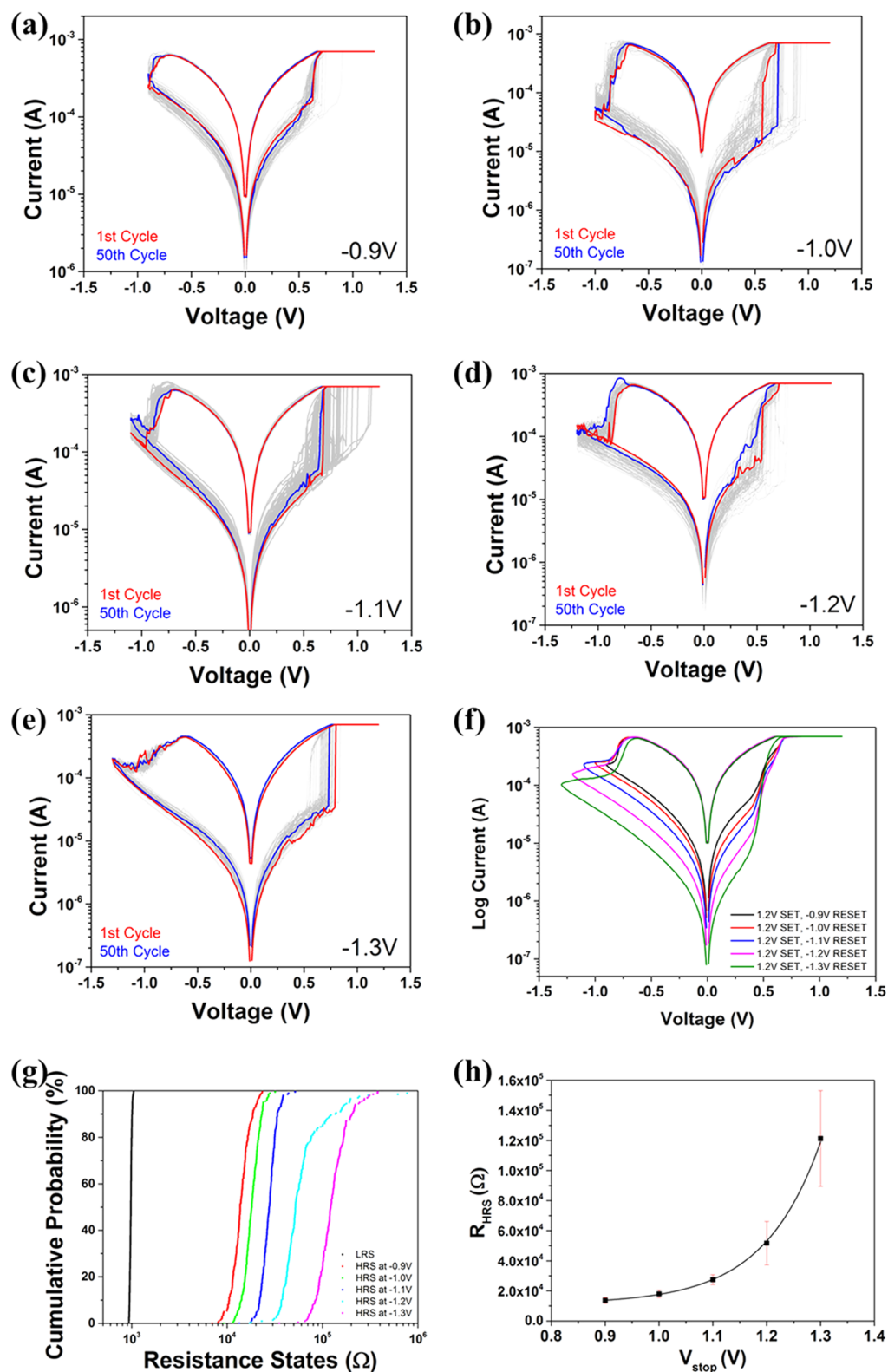
Figure 7. Semi-log $I-V$ plots of $Pt/HfO_2/Ti$ resistive switching devices with V_{stop} at (a) −0.9, (b) −1.0, (c) −1.1, (d) −1.2, and (e) −1.3 V, indicating an increasing HRS trend. (f) Mean of each semi-log $I-V$ plot from panels (a−e) and (g) their corresponding cumulative probability plot at $V_{read} = -0.1$ V of 200 $I-V$ cycles in each voltage of −0.9 to −1.3 V at intervals of −0.1 V. (h) R_{HRS} vs. V_{stop} with an exponential fit with 25th−75th percentile as the range of error bars.

performed on $Pt/HfO_2/Ti$ resistive switching devices and HfO_x films, respectively. TEM was performed on the devices to investigate the uniformity of deposited films and their crystallinity, while XPS studies were per-

formed on HfO_2 films to verify the Hf and O peaks. The TEM analysis in Figure 4a exhibited uniformly deposited RRAM layers with the inset of Figure 4a showing an amorphous HfO_x structure.

In the XPS profiles, broad and overlapping O 1s peaks and well-separated spin-orbit Hf 4f peaks were shown in Figure 4b and its inset, respectively.[38] The deconvolution of the Gaussian O 1s spectrum revealed two different oxygen components of binding energies 530.0 and 531.8 eV, respectively, as shown in Figure 4b. While the 530.0 eV peak is characteristic to O^{2-}, the higher binding energy of 531.8 eV can be attributed to V_o^{2+}.[39-41] The amount of oxygen vacancies was found to be 4.79% of the entire oxygen content of the HfO_x material by taking the proportion of areas under the two oxygen peaks in Figure 4b. Similarly, the binding energies of the Hf 4f peaks were found to be 16.8 and 18.3 eV as shown in the inset of Figure 4b, which were characteristic to Hf.[42] While Burrell et al. discussed about using spectral peak energy, intensity, and structural analysis to determine the composition and chemical state of the material species, Luo et al. performed XPS on their HfO_2 films by capturing the energy of X-ray-ejected photoemitted electrons specific to the chemical state and compounds. These analyses culminated in the area calculations under the material profiles such that by comparing the areas under the curve of the O 1s and Hf 4f profiles,[38,43,44] the atomic concentrations revealed a stoichiometry of HfO_2 with an error of 0.25%.[43,44]

◼ TEMPERATURE CHARACTERIZATION AND ARRHENIUS EQUATION RELATION BETWEEN THE HIGH RESISTANCE STATE AND TEMPERATURE

Various temperature studies were performed at −40, 25, 75, and 125 °C, and 50 cycles of I−V curves were measured at each temperature as shown in Figure 5a−d, respectively, with average curves in red.[51] The SET voltage ranged from 0.5 to 0.75 V, the RESET voltage was −1.2 V, while the ON/OFF ratio is about 50× at the same V_{read} at −0.1 V. The RESET processes have shown stable HRS switching and maintained ∼50× ON/OFF ratio at −40, 25, 75, and 125 °C. These observations indicated a good thermal stability in $Pt/HfO_2/Ti$ resistive switching devices in the HRS even at low temperatures, indicating that the multilevel HRS is resilient at different temperature ranges.

Further temperature studies at −40, 25, 75, 125, and 175 °C were also performed on devices 1, 2, and 3 to investigate the full operating range of $Pt/HfO_2/Ti$ RRAM devices. An I−V sweep of −0.6 to 0.6 V was performed on devices 1, 2, and 3 where the HRS decreases with an increasing temperature trend as shown in Figure 6a−c, respectively. For each of these devices, the HRS values were extracted at each temperature point at a randomly selected low V_{read} of 0.4 V. Thereafter, an Arrhenius equation indicated by eq 1 was linearly fitted on those extracted points as shown in Figure 6d by taking a natural logarithm on both sides of eq 1:

$$R_{HRS} = R_0 \exp\left(\frac{E_{AC}}{kT}\right), \tag{1}$$

where R_{HRS} is the HRS, R_0 is the pre-exponential factor, E_{AC} is the activation energy of HfO_2, k is the Boltzmann constant, and T is the corresponding temperature of the performed measurement. The value of R_0 is inversely related to n_D, which is indicative of the n_D present in $Pt/HfO_2/Ti$ devices and is characteristic to different RRAM stack configurations. Eq 1 shows that R_0 is proportional to R_{HRS}, thus making R_{HRS} inversely related to n_D. At the same time, eq 1 also shows that R_{HRS} is inversely proportional to temperature,[29] which would result in the increase in n_D with increasing temperature. More intuitively, n_D increases with increasing temperature because a

higher temperature lowers the resistance of the RRAM device, which increases n_D.[26,28,29,45] The decreased resistance of the device could be attributed to a less significant filament rupture, which in turn is caused by a higher n_D. A less significant rupture is represented by a lower extent of recombination between O^{2-} and V_o^{2+}, thus causing the density of V_o^{2+} to be higher, i.e., n_D is higher. E_{AC} and R_0 were found to exhibit average values of 0.022 eV and 152.18 Ω, respectively from the fittings shown in Figure 6d. The value of E_{AC} was also found to be at a consistent range to the values reported by Larcher et al. and Bersuker et al. for HfO_x-based devices.[46,47] The R_{HRS} versus $1/T$ trend has remained similar for all three devices, indicating that R_{HRS} increases with decreasing temperature.

◼ SWITCHING MODEL BETWEEN ACTIVATION ENERGY, RESET STOPPING VOLTAGE, AND RESET MULTILEVEL RESISTANCE STATES

The E_{AC} of HfO_2 was further investigated with n_D, which changes with V_{stop}. Multilevel states were explored by varying the V_{stop} from −0.9 to −1.3 V at intervals of −0.1 V as shown in Figure 7a−e, respectively. It could be observed that as the V_{stop} increases from −0.9 to −1.3 V, the HRS increases, and n_D decreases. Further investigations of the multilevel states were performed where 200 I−V cycles in each voltage of −0.9 to −1.3 V at intervals of −0.1 V shown in Figure 7a−e were averaged and combined into Figure 7f. Thereafter, the cumulative probability for all 200 I−V cycles shown in Figure 7a−e were plotted at V_{read} = −0.1 V in Figure 7g. It can also be observed from the cumulative probability plot in Figure 7g that the HRS increased at a faster rate as voltage increases. Therefore, an exponential factor between the HRS and V_{stop} could be used to explain the filament evolution and its relationship with multilevel states in eq 2:

$$R_{HRS} = \alpha \exp(\beta V_{stop}), \tag{2}$$

where R_{HRS} is again the HRS, α is the constant factor of the exponential function, and β is a factor of the exponent. R_{HRS} is plotted against V_{stop} in Figure 7h; α was found to be 86.34, and β was found to be 5.42 at the 50th percentile. The 25th and 75th percentiles were also plotted as the range of the error bars, mostly exhibiting non-overlap between different multilevel states. As eq 1 relates R_{HRS} to E_{AC} and eq 2 relates R_{HRS} to V_{stop}, which is a function of E_{AC}, the relationship between E_{AC} and V_{stop} can be established in eq 3 by combining eqs 1 and 2.

$$E_{AC} = [\ln(\alpha) - \ln(R_0)]kT + \beta V_{stop}kT \tag{3}$$

As the R_{HRS} versus V_{stop} measurement was performed at room temperature, eq 3 was simplified into eq 4 where γ and ϕ are constants:

$$E_{AC} = \gamma + \phi V_{stop} \tag{4}$$

Hence, a reduction in n_D due to increasing V_{stop} resulted in a higher R_{HRS}, which in turn resulted in a larger E_{AC} as shown in eq 4 was in line with the reported literature.[25,26] Intuitively, a larger filament rupture is caused by a larger V_{stop} due to more recombination between O^{2-} and V_o^{2+}, thus resulting in a lower n_D.

KINETIC MONTE CARLO SIMULATION WITH VARYING OXYGEN VACANCY DENSITY IN DIFFERENT REGIONS OF THE FILAMENT

kMC modeling was performed on $Pt/HfO_2/Ti$ devices using Ginestra, which applies comprehensive physics to simulate defect evolution, where the electric field and potential profiles were calculated by solving Poisson's and charge continuity equations.[48] The kMC model parameters obtained from the density functional theory (DFT) and literature were implemented. Generation, recombination, and diffusion of O^{2-} and V_o^{2+} are the main processes governing the filament evolution when V_{stop} was increased from 0 to -2 V. The assumptions of the kMC model include the following: (1) the full length of the filament runs from one end of the electrode to the other; (2) the filament gap during the rupture process is with respect to the top electrode; and (3) generation, recombination, and diffusion equations are used to describe oxygen ions and vacancies. These processes and model parameters were exhibited in the flowchart as shown in Figure 8.
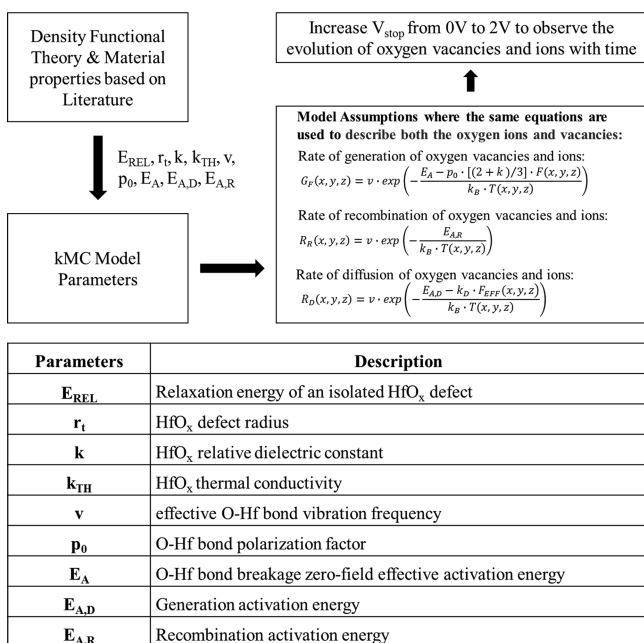
Figure 8. Modeling flow chart indicating the key processes and model parameters used to perform a kMC study on the behavior of oxygen vacancies at different V_{stop}.

In the generation of defects associated to the breakage of Hf−O bonds during the SET operation, the rate of generation of oxygen vacancies and ions G_F is calculated by the thermochemical theory as shown in eq 5.[49,50]

$$G_F(x, y, z) = v \cdot \exp\left(-\frac{E_A - p_0 \cdot [(2 + k)/3] \cdot F(x, y, z)}{k_B \cdot T(x, y, z)}\right)$$ (5)

where v is the effective vibration frequency, E_A is the zero field effective activation energy to break the metal-oxygen bond, F is the electric field, k_B is the Boltzmann's constant, p_0 is the dielectric molecular dipole moment, and k is the relative dielectric constant. Similarly, during RESET, the diffusion and recombination of carriers play an important role, and their rate can be calculated by eqs 6 and 7.[49]

$$R_D(x, y, z) = v \cdot \exp\left(-\frac{E_{A,D} - k_D \cdot F_{EFF}(x, y, z)}{k_B \cdot T(x, y, z)}\right)$$ (6)

$$R_R(x, y, z) = v \cdot \exp\left(-\frac{E_{A,R}}{k_B \cdot T(x, y, z)}\right)$$ (7)

where R_D is the diffusion rate, $E_{A,D}$ is the diffusion activation energy, k_D is a factor based on atomic material properties, F_{EFF} is the electric field component along the diffusion direction, R_R is the recombination rate, and $E_{A,R}$ is the recombination activation energy.[49,51,52] Table 1 also shows the model parameter values used in the kMC model simulation, obtained from the DFT and literature.

Table 1. Model Parameters Used in the kMC Model Obtained from the DFT and Literature

parameters	description	value	reference
	parameters obtained from the DFT and literature		
E_{REL}	relaxation energy of an isolated HfO_x defect	1.19 eV	53
r_t	HfO_x defect radius	5.64 Å	49
k	HfO_x relative dielectric constant	21	54
k_{TH}	HfO_x thermal conductivity	0.005 W/cm K	55
v	effective O−Hf bond vibration frequency	7×10^{13} Hz	56
p_0	O−Hf bond polarization factor	5.2 eÅ	56
E_A	O−Hf bond breakage zero-field effective activation energy	2.9 eV	56
$E_{A,D}$	generation activation energy	vacancies: 1.5 eV; ions: 0.7 eV	57
$E_{A,R}$	recombination activation energy	0.2 eV	58

In the validation of eq 4, a kMC simulation of $Pt/HfO_2/Ti$ devices considers the more general case of V_o^{2+} filament species during the RESET as shown in Figure 9a.[59−62] V_{stop} ranging from -1.2 to -2 V were simulated, and the number of oxygen vacancies (n_o) versus V_{stop} in Figure 9a revealed that n_o remained constant at the beginning. However, when V_{stop} is sufficient to overcome the oxide barrier, n_o decreases linearly until it eventually saturates at a certain number. For simplicity, the filament was separated into two regions, the top 25% of the filament and the bottom 75% of the filament. Further analysis of n_o at different locations of the filament at different V_{stop} were also performed where the n_o was obtained at the top 25% gap and bottom 75% non-gap regions of the filament as shown in Figure 9b. It was observed that n_o decreases in all parts of the filament as V_{stop} increases. The kMC simulation suggests that the rupture at the gap region becomes larger as V_{stop} is increased from -1.2 to -2 V, as shown in Figure 9b.[63−66] As n_o is proportional to n_D, the kMC model validates the inverse relationship between V_{stop} and n_D.

HOPPING CONDUCTION OF PT/HFO₂/TI RRAM DEVICES AND THE RELATION BETWEEN HOPPING DISTANCE AND RESET STOPPING VOLTAGE

While the filament rupture at the top 25% gap of the filament with increasing V_{stop} is well established, the decrease in n_D for the rest of the filament might not be as well understood. Therefore, the decrease in n_D for the bottom 75% of the filament was further investigated using conduction mechanism studies. Although Fowler−Nordheim (FN) tunneling has been considered as one of the candidates for conduction mechanism studies, hopping
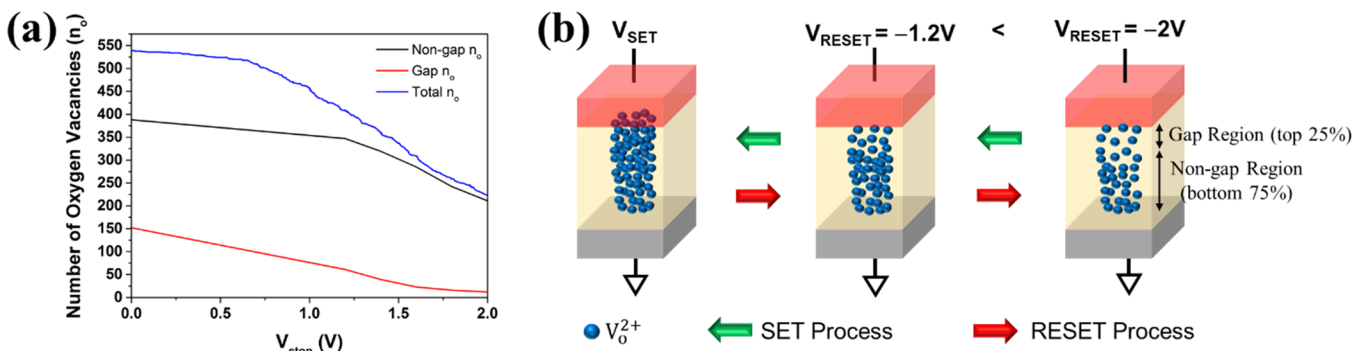
Figure 9. (a) Number of oxygen vacancies (n_o) vs. V_{stop} in all regions. (b) kMC model exhibiting the oxygen vacancy motion between SET and RESET processes where more rupture occurs at higher V_{stop}.

conduction as part of trap-assisted tunneling (TAT) is more suitable to interpret these results.[67] This is due to the focus of this work at high negative voltages and trap-to-trap characteristics at the bulk during the rupture process. In the fitting analysis, hopping conduction was found to be the dominant conduction mechanism for V_{stop} from −0.9 to −1.3 V as shown in Figure 10.
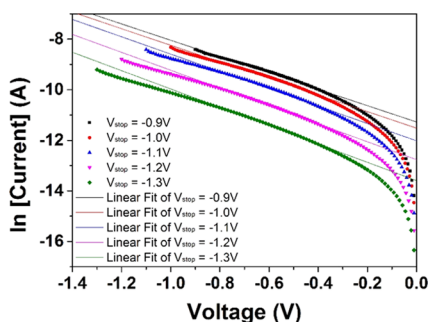
Figure 10. Hopping conduction fitting analysis of V_{stop} from −0.9 to −1.3 V.

The hopping conduction used for the analysis was shown in eq 8:

$$J = qanv\exp\left(\frac{qaE - \phi_T}{kT}\right) \tag{8}$$

where $n = 5 \times 10^{24}$ m^{-3} is the electron concentration in the conduction band,[68] $v = 2 \times 10^{13}$ Hz is the frequency of thermal vibration of electrons in the trap site,[69] a is the mean distance between traps, and ϕ_T is the energy level of the trap site below the conduction band.[70] The linear fitting of hopping conduction was performed by taking the natural log on eq 8 followed by an $\ln(I)$ versus V plot as shown in Figure 10. The selected fitting voltage range of −0.9 to −1.3 V with a corresponding current range of ∼2 orders exhibited a good fit with linear correlation. Unlike the abrupt SET process found in Pt/HfO$_2$/Ti RRAM devices, the gradual RESET switching process enabled the investigation of trap-to-trap characteristics at different V_{stop} and hence different multilevel states. The gradient (M) and vertical intercept (C) from eqs 9 and 10 can also be extracted from the fitting $\ln(I) = MV + C$:

$$M = \frac{qa}{kTd} \tag{9}$$

$$C = \ln(qanVa) - \frac{\phi_T}{kT} \tag{10}$$

where d is the distance between the top and bottom electrode, while a and ϕ_T can be obtained from eqs 9 and 10, respectively. The parameter a extracted from eqs 9 and 10 was shown to increase as V_{stop} increases from −0.9 to −1.3 V at intervals of −0.1 V in Table 2. As V_{stop} increases, V_o^{2+} became further apart as

Table 2. Hopping Distance (a) Extracted from Figure 10 at Different V_{stop} Indicated an Increasing Trend with Increasing V_{stop}

V_{stop} (V)	−0.9	−1.0	−1.1	−1.2	−1.3
trap-to-trap distance, a (nm)	0.83	0.84	0.88	0.91	0.93

indicated by the larger a to be overcome, thus resulting in a decrease in n_D, while ϕ_T remained fairly constant at 0.86 eV. As a larger a is caused by a less dense filament or lower n_D, the hopping conduction analysis also validates the inverse relationship between V_{stop} and n_D.

■ CONCLUSIONS

In conclusion, the multilevel resistance states of Pt/HfO$_2$/Ti RRAM devices obtained from increasing V_{stop} have shown to be directly related to E_{AC} but inversely related to n_D. The average E_{AC} value was extracted from an Arrhenius equation to be 0.022 eV at a wide temperature range of −40 to 175 °C and was shown to be inversely proportional to n_D as a part of our proposed switching model. The multilevel high resistance states were achieved at V_{stop} from −0.9 to −1.3 V at intervals of −0.1 V. In the validation of the relationship between n_D and V_{stop}, kMC simulations exhibited a decrease in n_D at increasing V_{stop} at different regions of the filament. The decrease in n_D at increasing V_{stop} was also attributed to a larger trap-to-trap distance to be overcome from 0.83 to 0.93 nm in the hopping conduction mechanism analysis. The uniformly fabricated Pt/HfO$_2$/Ti devices exhibited at least 5×10^5 endurance cycles at 100 ns with a retention for more than 10 years at 125 °C. With good thermal stability and multilevel state capabilities, Pt/HfO$_2$/Ti RRAM devices and their proposed models have great potential for neuromorphic engineering in automobiles.

■ AUTHOR INFORMATION

Corresponding Author

Wen Siang Lew − *School of Physical and Mathematical Sciences, Nanyang Technological University, Singapore 637371;*

 orcid.org/0000-0002-5161-741X; Email: wensiang@ntu.edu.sg

Authors

Desmond J. J. Loy − *School of Physical and Mathematical Sciences, Nanyang Technological University, Singapore 637371; Global foundries Singapore Pte Ltd, Singapore 738406;* orcid.org/0000-0001-7651-3214

Putu A. Dananjaya − *School of Physical and Mathematical Sciences, Nanyang Technological University, Singapore 637371;* orcid.org/0000-0001-9416-6455

Somsubhra Chakrabarti − *School of Physical and Mathematical Sciences, Nanyang Technological University, Singapore 637371*

Kuan Hong Tan − *School of Physical and Mathematical Sciences, Nanyang Technological University, Singapore 637371*

Samuel C. W. Chow − *School of Physical and Mathematical Sciences, Nanyang Technological University, Singapore 637371; Global foundries Singapore Pte Ltd, Singapore 738406*

Eng Huat Toh − *Global foundries Singapore Pte Ltd, Singapore 738406*

Complete contact information is available at:
https://pubs.acs.org/10.1021/acsaelm.0c00515

Author Contributions

The manuscript was written through contributions of all authors. D.J.J.L. conceived the idea and designed this work. D.J.J.L. performed most of the resistive switching device fabrication, characterizations, and analysis of results. D.J.J.L., P.A.D., and S.C.W.C. fabricated the devices, while P.A.D., S.C., and E.H.T. provided guidance and suggestions to this work. W.S.L. coordinated and supervised the entire work. All authors have given approval to the final version of the manuscript.

Notes

The authors declare no competing financial interest.

■ ABBREVIATIONS

$I-V$, current−voltage; E_{AC}, activation energy; V_{stop}, RESET stop voltage; V_o^{2+}, oxygen vacancy; n_D, oxygen vacancy density; HRS, high resistance state; kMC, kinetic Monte Carlo; TEM, transmission electron microscopy; XPS, X-ray photoelectron spectroscopy; RRAM, resistive random access memory; MIM, metal−insulator−metal; CMOS, complementary metal oxide semiconductor; V_{read}, read voltage; PVS, pulsed voltage stress; DFT, density functional theory; n_o, number of oxygen vacancies; FN, Fowler−Nordheim; TAT, trap-assisted tunneling

■ REFERENCES

(1) Wang, H.; Yan, X. Overview of Resistive Random Access Memory (RRAM): Materials, Filament Mechanisms, Performance Optimization, and Prospects. *Phys. Status Solidi RRL* **2019**, *13*, 1900073.

(2) Gupta, V.; Kapur, S.; Saurabh, S.; Grover, A. Resistive Random Access Memory: A Review of Device Challenges. *IETE Tech. Rev.* **2019**, 1−390.

(3) Goux, L. OxRAM technology development and performances. In *Advances in Non-volatile Memory and Storage Technology 2nd Edition*, Yoshio Nishi, B. M.-K., Ed. Woodhead Publishing: Duxfordm, UK, 2019; pp. 3−33.

(4) He, Z.-Y.; Wang, T.-Y.; Chen, L.; Zhu, H.; Sun, Q.-Q.; Ding, S.-J.; Zhang, D. W. Atomic Layer-Deposited HfAlOx-Based RRAM with Low Operating Voltage for Computing In-Memory Applications. *Nanoscale Res. Lett.* **2019**, *14*, 51.

(5) Rainer Waser, D. I., Hiro, Akinaga, Hisashi, Shima, H.-S. Philip, Wong, Joshua J., Yang, Simon, Yu Introduction to Nanoionic Elements for Information Technology. In *Resistive Switching: From Fundamentals of Nanoionic Redox Processes to Memristive Device Applications*, Daniele Ielmini, R. W., Ed. Wiley: Hoboken, NJ, USA, 2016; pp. 1−30.

(6) Loy, D. J. J.; Dananjaya, P. A.; Hong, X. L.; Shum, D. P.; Lew, W. S. Conduction Mechanisms on High Retention Annealed MgO-based Resistive Switching Memory Devices. *Sci. Rep.* **2018**, *8*, 14774.

(7) Wong, H. P.; Lee, H.; Yu, S.; Chen, Y.; Wu, Y.; Chen, P.; Lee, B.; Chen, F. T.; Tsai, M. Metal−Oxide RRAM. *Proc. IEEE* **2012**, *100*, 1951−1970.

(8) Ielmini, D. Resistive switching memories based on metal oxides: mechanisms, reliability and scaling. *Semicond. Sci. Technol.* **2016**, *31*, No. 063002.

(9) Valov, I.; Waser, R.; Jameson, J. R.; Kozicki, M. N. Electrochemical metallization memories—fundamentals, applications, prospects. *Nanotechnology* **2011**, *22*, 254003.

(10) Wedig, A.; Luebben, M.; Cho, D.-Y.; Moors, M.; Skaja, K.; Rana, V.; Hasegawa, T.; Adepalli, K. K.; Yildiz, B.; Waser, R.; Valov, I. Nanoscale cation motion in TaOx, HfOx and TiOx memristive systems. *Nat. Nanotechnol.* **2016**, *11*, 67−74.

(11) Privitera, S.; Bersuker, G.; Butcher, B.; Kalantarian, A.; Lombardo, S.; Bongiorno, C.; Geer, R.; Gilmer, D. C.; Kirsch, P. D. Microscopy study of the conductive filament in HfO2 resistive switching memory devices. *Microelectron. Eng.* **2013**, *109*, 75−78.

(12) Chandrasekaran, S.; Simanjuntak, F. M.; Aluguri, R.; Tseng, T.-Y. The impact of TiW barrier layer thickness dependent transition from electro-chemical metallization memory to valence change memory in ZrO2-based resistive switching random access memory devices. *Thin Solid Films* **2018**, *660*, 777−781.

(13) Lanza, M. A Review on Resistive Switching in High-k Dielectrics: A Nanoscale Point of View Using Conductive Atomic Force Microscope. *Materials* **2014**, *7*, 2155−2182.

(14) Liu, C.-F.; Tang, X.-G.; Wang, L.-Q.; Tang, H.; Jiang, Y.-P.; Liu, Q.-X.; Li, W.-H.; Tang, Z.-H. Resistive Switching Characteristics of HfO2 Thin Films on Mica Substrates Prepared by Sol-Gel Process. *Nanomaterials* **2019**, *9*, 1−11.

(15) Milo, V.; Zambelli, C.; Olivo, P.; Pérez, E.; Mahadevaiah, M. K.; Ossorio, O. G.; Wenger, C.; Ielmini, D. Multilevel HfO2-based RRAM devices for low-power neuromorphic networks. *APL Mater.* **2019**, *7*, No. 081120.

(16) Gao, B.; Liu, L.; Kang, J. Investigation of the synaptic device based on the resistive switching behavior in hafnium oxide. *Prog. Nat. Sci.: Mater. Int.* **2015**, *25*, 47−50.

(17) Jain, B.; Huang, C.-S.; Misra, D.; Tapily, K.; Clark, R. D.; Consiglio, S.; Wajda, C. S.; Leusink, G. J. Multilevel Resistive Switching in Hf-Based RRAM. *ECS Trans.* **2019**, *89*, 39−44.

(18) Chang, T.-C.; Chang, K.-C.; Tsai, T.-M.; Chu, T.-J.; Sze, S. M. Resistance random access memory. *Mater. Today* **2016**, *19*, 254−264.

(19) Gupta, M.; Kedia, J. A Review on Resistive Random Access Memory. *Int. J. Adv. Res. Electron. Commun. Eng.* **2018**, *7*, 184−191.

(20) Shirinzadeh, S.; Drechsler, R. In-Memory Computing: The Integration of Storage and Processing. In *Information Storage − A Multidisciplinary Perspective*, Cornelia, S.; Große, R. D., Ed. Springer Nature: Basel, Switzerland, 2020; pp. 79−110.

(21) Ielmini, D. Brain-inspired computing with resistive switching memory (RRAM): Devices, synapses and neural networks. *Microelectron. Eng.* **2018**, *190*, 44−53.

(22) Ielmini, D.; Ambrogio, S. Neuromorphic computing with resistive switching memory devices. In *Advances in Non-volatile Memory*

and Storage Technology 2nd Edition, Yoshio Nishi, B. M.-K., Ed. Woodhead Publishing: Duxford, UK, 2019; pp. 3−33.

(23) Moon, K.; Lim, S.; Park, J.; Sung, C.; Oh, S.; Woo, J.; Lee, J.; Hwang, H. RRAM-based synapse devices for neuromorphic systems. *Faraday Discuss.* **2019**, *213*, 421−451.

(24) Ielmini, D. Modeling the Universal Set/Reset Characteristics of Bipolar RRAM by Field- and Temperature-Driven Filament Growth. *IEEE Trans. Electron Devices* **2011**, *58*, 4309−4317.

(25) Bousoulas, P.; Asenov, P.; Karageorgiou, I.; Sakellaropoulos, D.; Stathopoulos, S.; Tsoukalas, D. Engineering amorphous-crystalline interfaces in TiO_{2-x}/TiO_{2-y}-based bilayer structures for enhanced resistive switching and synaptic properties. *J. Appl. Phys.* **2016**, *120*, 154501.

(26) Larentis, S.; Nardi, F.; Balatti, S.; Gilmer, D. C.; Ielmini, D. Resistive Switching by Voltage-Driven Ion Migration in Bipolar RRAM—Part II: Modeling. *IEEE Trans. Electron Devices* **2012**, *59*, 2468−2475.

(27) Kim, S.; Kim, S.-J.; Kim, K. M.; Lee, S. R.; Chang, M.; Cho, E.; Kim, Y.-B.; Kim, C. J.; In Chung, U.; Yoo, I.-K. Physical electro-thermal model of resistive switching in bi-layered resistance-change memory. *Sci. Rep.* **2013**, *3*, 1680.

(28) Chiu, F.-C.; Li, P.-W.; Chang, W.-Y. Reliability characteristics and conduction mechanisms in resistive switching memory devices using ZnO thin films. *Nanoscale Res. Lett.* **2012**, *7*, 178.

(29) Khurana, G.; Misra, P.; Katiyar, R. S. Forming free resistive switching in graphene oxide thin film for thermally stable nonvolatile memory applications. *J. Appl. Phys.* **2013**, *114*, 124508.

(30) Chakrabarti, S.; Ginnaram, S.; Jana, S.; Wu, Z.-Y.; Singh, K.; Roy, A.; Kumar, P.; Maikap, S.; Qiu, J.-T.; Cheng, H.-M.; Tsai, L.-N.; Chang, Y.-L.; Mahapatra, R.; Yang, J.-R. Negative voltage modulated multi-level resistive switching by using a Cr/BaTiOx/TiN structure and quantum conductance through evidence of H_2O_2 sensing mechanism. *Sci. Rep.* **2017**, *7*, 4735.

(31) Samanta, S.; Rahaman, S. Z.; Roy, A.; Jana, S.; Chakrabarti, S.; Panja, R.; Roy, S.; Dutta, M.; Ginnaram, S.; Prakash, A.; Maikap, S.; Cheng, H.-M.; Tsai, L.-N.; Qiu, J.-T.; Ray, S. K. Understanding of multi-level resistive switching mechanism in GeOx through redox reaction in H_2O_2/sarcosine prostate cancer biomarker detection. *Sci. Rep.* **2017**, *7*, 11240.

(32) Bai, Y.; Wu, H.; Wu, R.; Zhang, Y.; Deng, N.; Yu, Z.; Qian, H. Study of Multi-level Characteristics for 3D Vertical Resistive Switching Memory. *Sci. Rep.* **2014**, *4*, 5780.

(33) Qi, M.; Guo, C.; Zeng, M. Oxygen Vacancy Kinetics Mechanism of the Negative Forming-Free Process and Multilevel Resistance Based on Hafnium Oxide RRAM. *J. Nanomater.* **2019**, *2019*, 1−9.

(34) Zahoor, F.; Azni Zulkifli, T. Z.; Khanday, F. A. Resistive Random Access Memory (RRAM): an Overview of Materials, Switching Mechanism, Performance, Multilevel Cell (mlc) Storage, Modeling, and Applications. *Nanoscale Res. Lett.* **2020**, *15*, 90.

(35) Oh, J.-H.; Ryoo, K.-C.; Jung, S.; Park, Y.; Park, B.-G. Effect of Oxidation Amount on Gradual Switching Behavior in Reset Transition of Al/TiO_2-Based Resistive Switching Memory and Its Mechanism for Multilevel Cell Operation. *Jpn. J. Appl. Phys.* **2012**, *51*, No. 04DD16.

(36) Lanza, M.; Wong, H.-S. P.; Pop, E.; Ielmini, D.; Strukov, D.; Regan, B. C.; Larcher, L.; Villena, M. A.; Yang, J. J.; Goux, L.; Belmonte, A.; Yang, Y.; Puglisi, F. M.; Kang, J.; Magyari-Köpe, B.; Yalon, E.; Kenyon, A.; Buckwell, M.; Mehonic, A.; Shluger, A.; Li, H.; Hou, T.-H.; Hudec, B.; Akinwande, D.; Ge, R.; Ambrogio, S.; Roldan, J. B.; Miranda, E.; Suñe, J.; Pey, K. L.; Wu, X.; Raghavan, N.; Wu, E.; Lu, W. D.; Navarro, G.; Zhang, W.; Wu, H.; Li, R.; Holleitner, A.; Wurstbauer, U.; Lemme, M. C.; Liu, M.; Long, S.; Liu, Q.; Lv, H.; Padovani, A.; Pavan, P.; Valov, I.; Jing, X.; Han, T.; Zhu, K.; Chen, S.; Hui, F.; Shi, Y. Recommended Methods to Study Resistive Switching Devices. *Adv. Electron. Mater.* **2019**, *5*, 1800143.

(37) Lee, M.-J.; Lee, C. B.; Lee, D.; Lee, S. R.; Chang, M.; Hur, J. H.; Kim, Y.-B.; Kim, C.-J.; Seo, D. H.; Seo, S.; Chung, U. I.; Yoo, I.-K.; Kim, K. A fast, high-endurance and scalable non-volatile memory device made from asymmetric Ta_2O_{5-x}/TaO_{2-x} bilayer structures. *Nat. Mater.* **2011**, *10*, 625−630.

(38) Burrell, M. C. Chemical Analysis, Electron Spectroscopy. In *Encyclopedia of Materials: Science and Technology*, Buschow, K. H. J.; Cahn, R. W.; Flemings, M. C.; Ilschner, B.; Kramer, E. J.; Mahajan, S.; Veyssière, P., Eds. Elsevier: Oxford, 2001; pp. 1142−1149, DOI: 10.1016/B0-08-043152-6/00214-X.

(39) Jain, S.; Shah, J.; Negi, N. S.; Sharma, C.; Kotnala, R. K. Significance of interface barrier at electrode of hematite hydroelectric cell for generating ecopower by water splitting. *Int. J. Energy Res.* **2019**, *43*, 4743−4755.

(40) Gan, J.; Lu, X.; Wu, J.; Xie, S.; Zhai, T.; Yu, M.; Zhang, Z.; Mao, Y.; Wang, S. C. I.; Shen, Y.; Tong, Y. Oxygen vacancies promoting photoelectrochemical performance of In_2O_3 nanocubes. *Sci. Rep.* **2013**, *3*, 1021−1021.

(41) Lu, X.; Zeng, Y.; Yu, M.; Zhai, T.; Liang, C.; Xie, S.; Balogun, M.-S.; Tong, Y. Oxygen-Deficient Hematite Nanorods as High-Performance and Novel Negative Electrodes for Flexible Asymmetric Supercapacitors. *Adv. Mater.* **2014**, *26*, 3148−3155.

(42) Zhang, L.; Liu, M.; Ren, W.; Zhou, Z.; Dong, G.; Zhang, Y.; Peng, B.; Hao, X.; Wang, C.; Jiang, Z.-D.; Jing, W.; Ye, Z.-G. ALD preparation of high-k HfO_2 thin films with enhanced energy density and efficient electrostatic energy storage. *RSC Adv.* **2017**, *7*, 8388−8393.

(43) David, D.; Godet, C. Derivation of dielectric function and inelastic mean free path from photoelectron energy-loss spectra of amorphous carbon surfaces. *Appl. Surf. Sci.* **2016**, *387*, 1125−1139.

(44) Luo, X.; Li, Y.; Yang, H.; Liang, Y.; He, K.; Sun, W.; Lin, H.-H.; Yao, S.; Lu, X.; Wan, L.; Feng, Z. Investigation of HfO_2 Thin Films on Si by X-ray Photoelectron Spectroscopy, Rutherford Backscattering, Grazing Incidence X-ray Diffraction and Variable Angle Spectroscopic Ellipsometry. *Crystals* **2018**, *8*, 248.

(45) Puglisi, F. M.; Qafa, A.; Pavan, P. Temperature Impact on the Reset Operation in HfO_2 RRAM. *IEEE Electron Device Lett.* **2015**, *36*, 244−246.

(46) Larcher, L.; Puglisi, F. M.; Pavan, P.; Padovani, A.; Vandelli, L.; Bersuker, G. A Compact Model of Program Window in HfO_x RRAM Devices for Conductive Filament Characteristics Analysis. *IEEE Trans. Electron Devices* **2014**, *61*, 2668−2673.

(47) Bersuker, G.; Gilmer, D. C.; Veksler, D.; Kirsch, P.; Vandelli, L.; Padovani, A.; Larcher, L.; McKenna, K.; Shluger, A.; Iglesias, V.; Porti, M.; Nafría, M. Metal oxide resistive memory switching mechanism based on conductive filament properties. *J. Appl. Phys.* **2011**, *110*, 124518.

(48) *Ginestra™, A. M. APPLIED MDLX™ GINESTRA™ SIMU-LATION SOFTWARE*. http://www.appliedmaterials.com/products/applied-mdlx-ginestra-simulation-software.

(49) Padovani, A.; Larcher, L.; Pirrotta, O.; Vandelli, L.; Bersuker, G. Microscopic Modeling of HfOx RRAM Operations: From Forming to Switching. *IEEE Trans. Electron Devices* **2015**, *62*, 1998−2006.

(50) Padovani, A.; Larcher, L. In *Time-dependent dielectric breakdown statistics in SiO2 and HfO2 dielectrics: Insights from a multi-scale modeling approach*, 2018 IEEE International Reliability Physics Symposium (IRPS), 11−15 March 2018; 2018; pp. 3A.2-1-3A.2-7.

(51) Larcher, L.; Padovani, A. Multiscale modeling of oxide RRAM devices for memory applications: from material properties to device performance. *J. Comput. Electron.* **2017**, *16*, 1077−1084.

(52) Puglisi, F. M.; Larcher, L.; Padovani, A.; Pavan, P. Bipolar Resistive RAM Based on HfO_2: Physics, Compact Modeling, and Variability Control. *IEEE J. Emerging Sel. Top. Circuits Syst.* **2016**, *6*, 171−184.

(53) Vandelli, L.; Padovani, A.; Larcher, L.; Southwick, R. G.; Knowlton, W. B.; Bersuker, G. A Physical Model of the Temperature Dependence of the Current Through SiO_2/HfO_2 Stacks. *IEEE Trans. Electron Devices* **2011**, *58*, 2878−2887.

(54) Rahman, M. M.; Kim, J. G.; Kim, D. H.; Kim, T. W. Characterization of Al Incorporation into HfO_2 Dielectric by Atomic Layer Deposition. *Micromachines* **2019**, *10*, 361.

(55) Panzer, M. A.; Shandalov, M.; Rowlette, J. A.; Oshima, Y.; Chen, Y. W.; McIntyre, P. C.; Goodson, K. E. Thermal Properties of Ultrathin Hafnium Oxide Gate Dielectric Films. *IEEE Electron Device Lett.* **2009**, *30*, 1269−1271.

(56) Padovani, A.; Larcher, L.; Bersuker, G.; Pavan, P. Charge Transport and Degradation in HfO_2 and HfO_x Dielectrics. *IEEE Electron Device Lett.* **2013**, *34*, 680−682.

(57) Foster, A. S.; Shluger, A. L.; Nieminen, R. M. Mechanism of Interstitial Oxygen Diffusion in Hafnia. *Phys. Rev. Lett.* **2002**, *89*, 225901.

(58) Govindaraj, R.; Sundar, C. S.; Kesavamoorthy, R. Atomic scale study of oxidation of hafnium: Formation of hafnium core and oxide shell. *J. Appl. Phys.* **2006**, *100*, No. 084318.

(59) Dai, Y.; Pan, Z.; Wang, F.; Li, X. Oxygen vacancy effects in HfO2-based resistive switching memory: First principle study. *AIP Adv.* **2016**, *6*, No. 085209.

(60) Calka, P.; Sowinska, M.; Bertaud, T.; Walczyk, D.; Dabrowski, J.; Zaumseil, P.; Walczyk, C.; Gloskovskii, A.; Cartoixà, X.; Suñé, J.; Schroeder, T. Engineering of the Chemical Reactivity of the Ti/HfO_2 Interface for RRAM: Experiment and Theory. *ACS Appl. Mater. Interfaces* **2014**, *6*, 5056−5060.

(61) Lu, Y.; Lee, J. H.; Chen, I. W. Scalability of voltage-controlled filamentary and nanometallic resistance memory devices. *Nanoscale* **2017**, *9*, 12690−12697.

(62) Thammasack, M.; Micheli, G.; Gaillardon, P.-E. Effect of O^{2-} migration in $Pt/HfO_2/Ti/Pt$ structure. *J. Electroceram.* **2017**, *39*, 137−142.

(63) Wu, X.; Mei, S.; Bosman, M.; Raghavan, N.; Zhang, X.; Cha, D.; Li, K.; Pey, K. L. Evolution of Filament Formation in Ni/HfO2/SiOx/Si-Based RRAM Devices. *Adv. Electron. Mater.* **2015**, *1*, 1500130.

(64) Shin, J.; Park, J.; Lee, J.; Park, S.; Kim, S.; Lee, W.; Kim, I.; Lee, D.; Hwang, H. Effect of Program/Erase Speed on Switching Uniformity in Filament-Type RRAM. *IEEE Electron Device Lett.* **2011**, *32*, 958−960.

(65) Bai, Y.; Wu, H.; Zhang, Y.; Wu, M.; Zhang, J.; Deng, N.; Qian, H.; Yu, Z. Low power W:AlOx/WOx bilayer resistive switching structure based on conductive filament formation and rupture mechanism. *Appl. Phys. Lett.* **2013**, *102*, 173503.

(66) Li, C.; Gao, B.; Yao, Y.; Guan, X.; Shen, X.; Wang, Y.; Huang, P.; Liu, L.; Liu, X.; Li, J.; Gu, C.; Kang, J.; Yu, R. Direct Observations of Nanofilament Evolution in Switching Processes in HfO(2) -Based Resistive Random Access Memory by In Situ TEM Studies. *Adv. Mater.* **2017**, *29*, 1602976.

(67) Gehring, A.; Selberherr, S. Modeling of tunneling current and gate dielectric reliability for nonvolatile memory devices. *IEEE Trans. Device Mater. Reliab.* **2004**, *4*, 306−319.

(68) Gritsenko, V. A.; Islamov, D. R.; Perevalov, T. V.; Aliev, V. S.; Yelisseyev, A. P.; Lomonova, E. E.; Pustovarov, V. A.; Chin, A. Oxygen Vacancy in Hafnia as a Blue Luminescence Center and a Trap of Charge Carriers. *J. Phys. Chem. C* **2016**, *120*, 19980−19986.

(69) Dominguez, O.; McGinnity, T. L.; Roeder, R. K.; Hoffman, A. J. Optical characterization of polar HfO_2 nanoparticles in the mid- and far-infrared. *Appl. Phys. Lett.* **2017**, *111*, No. 011101.

(70) Loy, D. J. J.; Dananjaya, P. A.; Law, W. C.; Lim, G. J.; Tan, F.; Hong, X. L.; Chow, S. C. W.; Toh, E. H.; Lew, W. S. In *Hopping Conduction Temperature Investigations on High Retention Electrochemical Metallization MgO-based Resistive Switching Devices in the Low Resistance State*, 2019 Electron Devices Technology and Manufacturing Conference (EDTM), 12−15 March 2019; 2019; pp. 163−165.